Power Electronic Systems
Laboratory

IET Electric Power Applications, pp. 1-9, October 2018

Weight Optimisation of Coreless Axial-Flux Permanent Magnet Machines

I. Subotic,
Ch. Gammeter,
A. Tüysüz,
J. W. Kolar

Eidgenössische Technische Hochschule Zürich
Swiss Federal Institute of Technology Zurich

Weight Optimization of Coreless Axial-Flux PM Machines

Ivan Subotic[1,2*], Christoph Gammeter[1,3], Arda Tüysüz[1], Johann W. Kolar[1]

[1] Power Electronic Systems Laboratory, ETH Zurich, 8092 Zurich, Switzerland
[2] Current affiliation: Dep. of Electronics and Electrical Eng., Liverpool John Moores Uni., Liverpool L3 3AF, UK
[3] Current affiliation: Celeroton AG, 8604 Volketswil, Switzerland
[*] i.subotic@ljmu.ac.uk

Abstract— This paper explores the upper limits in power-to-weight and torque-to-weight ratios of coreless axial-flux machines with permanent magnets. Moreover, it provides a comprehensive multifunctional optimization procedure that is utilized for obtaining these limits. The procedure encompasses analytical analysis of electro-magnetic, thermal and structural (mechanical) aspects of axial-flux machines. Obtaining global minima is ensured by considering the whole machine design space, and mapping it into the performance space, where a Pareto front can be easily identified. From it, an optimal motor/generator for airborne wind turbines is identified. The design has a power-to-weight ratio of 6.4 kW/kg (19 Nm/kg at 3200 rpm) including structural (purely mechanical) parts, at an efficiency of 95%. This is a significantly higher ratio than the one in modern commercial machines or designs reported in literature. Therefore, the resulting machine is manufactured and experimentally tested in order to verify the claimed limits and the optimization methodology.

1. Introduction

Airborne wind turbines (AWTs) are wind turbines (WTs) that do not have a rigid connection with the ground [1]. Their absence of a supporting tower or lengthy rotor blades leads to a much lower weight, and, therefore, to significant investment cost savings compared to traditional WTs of the same power (Fig. 1).

Although the scientific community has been aware of these advantages for more than four decades [2], its practical realization has just recently been made feasible with advancements in the areas of novel materials (light-weight, high-strength) and digital control methods (performing thousands of real-time operations) [3-4]. This created a demand for a power-to-weight optimization of all AWT elements [5].

This paper focuses on optimization of only one AWT element, a machine. Due to their high torque density [6], it considers only coreless axial-flux machines (CL-AFMs). It should be noted that although this paper focuses on AWTs, the analysis presented in the paper is also applicable to future electric aircrafts. Machine weight optimization for such applications has recently gained popularity both in academia and in industry [7]. In these applications weight savings should be made even if this is on the expense of a higher cost of active materials (usually PMs). The reason is a high cost of keeping the machine weight in the air.

There are various methods based on which an optimization of a machine design can be performed [8]. One of the most popular is by minimizing cost functions. On the other hand, defining cost functions can be a complex task, which especially holds true for multi-objective optimizations in which multiple performance indicators such as power-to-weight ratio and efficiency have to be taken into account [9]. An atypical method, which conveniently performs multi-objective optimisation is reported in [10]. Finally, cost functions commonly introduce a risk of a convergence to a local, rather than the global optimum [11].

A direct grid search, on the other hand, is a method that covers all possible machine designs, and this is a method that is employed in this paper. The complete design space is taken into consideration, which eliminates a need for cost functions. The design space has to be discretized as a trade-off between a computational effort and a precision of the outcome.

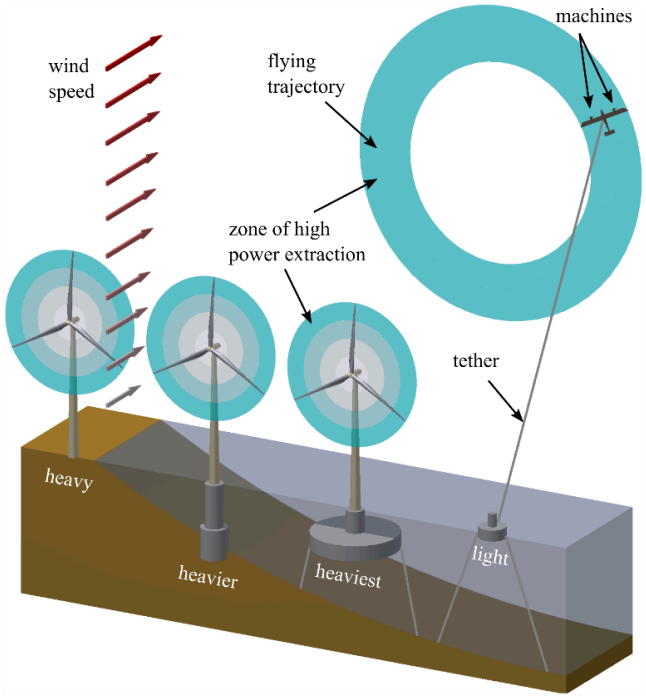

Fig. 1. *Qualitative weight comparison between (from the left to the right-hand side): a land based wind turbine (WT), shallow water WT, deep water WT and airborne wind turbine (AWT). Compared to other WT types, AWT has access to stronger winds and it extracts energy from a much larger surface. It emulates the behaviour of rotor blade tips of standard WT, but on a larger diameter. Thus, the whole flying trajectory is in a uniform power zone (zone of high power extraction). As a result, AWT weight of materials is multiple times lower compared to other WT types with the same rated power [3].*

In general, there are three manners of performing the direct grid search: by finite element models (FEM) [12], by analytical models, or by their combination. While 3D FEM has high accuracy, its slow execution restricts the number of machine designs that can be evaluated in a given time. Although employment of modified 2D AFM models [13] can be utilized to substantially reduce the execution time (on the

expense of somewhat higher error), it still remains relatively high. Therefore, analytical machine models, which are available in literature [14, 15], are more suitable for this kind of optimization.

A theoretical consideration of the weight optimization process of electrical machines in general was performed in [16]. However, machines with phase group windings (providing high pitch factor, excellent isolation between phases and easier manufacturability) were not considered. A weight optimization of AFMs including those with phase group windings is performed in [17]. Although [17] contains a very brief sample of experimental results, the analysis was done mainly on the theoretical level.

This paper provides a comprehensive analysis of power-to-weight ratio of different CL-AFMs, including those with phase group windings. The paper:

i) Offers a complete multi-objective machine optimization procedure that contains machine's electromagnetic, thermal and structural analysis.
ii) Provides clear upper limits in power-to-weight and torque-to-weight ratio of CL-AFMs for AWTs (and future electric aircrafts). The considered power is 12.5 kW (for higher powers the power-to-weight ratio is higher). Despite the increasing demand, at present, these limits are regarded as not well known.
iii) Verifies the obtained analytical and FEM results on a prototype machine for which a complete manufacturing procedure is given.

The paper is organized as follows. The optimization procedure is detailed in Section 2 and all degrees of freedom (DoF) of CL-AFM designs are defined. The CL-AFMs that are considered in the paper are identified. Section 3 gives an overview of the analytical models covering electro-magnetic, thermal and structural (mechanical) aspects of CL-AFMs. Based on these, performances of the CL-AFMs that are defined in Section 2 are evaluated in Section 4. Section 5 reveals the manufacturing procedure of CL-AFMs. Experimental verification of analytical models from Section 3 and theoretical results from Section 4 are given in Section 6.

2. Degrees of Freedom of the Machine Design

2.1. Optimization Procedure

This subsection describes a direct grid search optimization procedure that is utilized in this paper. The procedure contains the followings steps in a chronological order:

i) At first all degrees of freedom (Tables 2-3) and constraints (Table 1) in the machine designing process are identified.
ii) Then, for each degree of freedom a range of values that should be considered is identified (Sections 2.3, *2.4*).
iii) All possible combinations of values of the degrees of freedom (that are identified in steps 1-2) are made. Each combination fully and uniquely defines one machine design. Upper and lower values of each degree of freedom are selected in such way so that they lead to a meaningful machine design.
iv) Performances of each machine design (identified in step iii) are obtained from analytical models (given in Section 3), which consider their electromagnetic, thermal and structural aspects. Therefore, each specific feasible design, i.e. finally the whole design space, is mapped into a performance space. The two main performance indicators that are of importance in the case at hand are the machine's power-to-weight ratio and its efficiency.
v) Once the performance space containing those performance indicators of all the considered machines is obtained (Section 4), a group of superior designs can be easily recognized on the so-called Pareto front. The Pareto front is formed by a selection of analysed machines, whose efficiency and power density cannot be increased at the same time (one of them can only be increased by sacrificing the other).
vi) Finally, from machine designs on the Pareto front, one design that is the most appropriate for the given application is selected.

Table 1 Fixed parameters of the machine

Fixed parameter	Value (or design)
Machine type	Dual rotor with single stator,
Number of stacks	1
Stator type	Coreless
Permanent magnet material	NdFeB (B_r = 1.25 T)
Back iron material	CoFe (with Halbach not required)
Fill factor [-]	k_{Cu} = 0.55 for distributed windings, k_{Cu} = 0.85 for concentrated windings (based on [18] and manufacturability)
Air gap [mm]	1
Rated speed [rpm]	3200
Rated power [kW]	12.5
Cooling	Forced air at v = 55 m/s [3] (t_{inlet} = 25˚C)
Cooling flow rate [dm^3/s]	7 (takes into account AWT cruising speed)

Table 2 Rotor degrees of freedom and their considered values

DoF	Considered values (or designs)
Magnetization type	Axial with back iron (Fig. 2b), Halbach without iron (Fig. 2c)
Pole pair number [-]	p = 19 + {0, 1, 2, …7}
Disk inner radius [mm]	r_1 = 80 + 10·{0, 1, 2, …5}
Disk outer radius [mm]	r_2 = 90 + 5·{0, 1, 2, …14}
Permanent magnet height [mm]	h_m = {1, 2, 3, 4, 5}
Pole coverage of axial magnets [-]	α_p = {0.5, 0.6, 0.7, 0.8}
Back iron height [mm]	h_{Fe} = {1, 2, 3, 4, 5}

Table 3 Stator degrees of freedom and their considered values

DoF	Considered values (or designs)
Winding type	Distributed (Fig. 2d), Traditional concentrated (Fig. 2e), Phase group concentrated (Fig. 2f)
Number of coils	Q = 36 +3·{0, 1, 2, …14}
Coil height [mm]	c_h = {1, 2, 3, 4}
Fractional coil width [-]	$c_{\omega,\mathrm{frac}} = \frac{2c_\omega}{c_{\omega,\max}} = 0.45 + 0.1 \cdot \{0,1,...4\}$
Coil material	Copper, Aluminium
Current waveform	Sinusoidal (BLAC), Block (rectangular – BLDC)

2.2. Fixed Parameters

Some DoF have a clear optimum value for a selected optimization process. Whenever this is the case, only their optimal values should be considered. Machines with a double

rotor and a single stator (Fig. 2a) have superior performance in terms of power-to-weight ratio compared to single rotor AFMs [6, 19]. Therefore, only this type of machines is considered in what follows. Stacking of AFMs, which is a "no-tooling-cost" method for upscaling the power output of a given design, is not considered in this paper for the sake of brevity. Stators with air cores are exclusively considered, which is justified by their low weight and absence of iron losses and cogging torque [6]. The choice for the PM material is fixed to neodymium iron boron (NdFeB), and for the back iron to cobalt iron (CoFe). Although CoFe has a 4% higher mass density compared to silicon iron (SiFe), its selection is well justified by its high saturation flux density (2.3 T versus 1.8 T of SiFe). The air speed of 55m/s is a constraint dictated by the application. However, in other applications similar values of a resulting cooling flow rate can be obtained by introducing rotor fan blades [20]. The fixed parameters are summarized in Table 1.

2.3. Rotor DoF

Rotors can take two distinctive forms. One contains PMs magnetized only in the axial direction. In this form, a phase shift between each two adjacent magnets is 180 degrees and a back iron is utilized to strengthen the field that is produced by the PMs, cf. Fig. 2b.

The second rotor form contains PMs arranged in a segmented Halbach array, in which a phase shift between each two adjacent magnets is 90 degrees. It is well known that this type does not require a back iron to strengthen the field (although then the flux on the back side of PMs is not exactly zero). Therefore, this form is only considered without a back iron (Fig. 2c). All rotor DoF are summarized in Table 2.

High numbers of pole pairs (between 19 and 26) are considered, as they increase flux linkage. Although they can cause high skin effect losses, the effect can be suppressed after the Pareto optimization by appropriate selections of series and parallel turns of stator windings. The number 26 is taken as a limit for retaining easy manufacturability.

2.4. Stator DoF

Three types of windings can be employed in the stator: distributed (DW - Fig. 2d), traditional concentrated (TCW - Fig. 2e, [21]) or phase group concentrated windings (PGCW - Fig. 2f, [6]). The number of coils (Q) is selected as $Q = 3p$ in DW, and $Q = 2p\pm1$ in PGCW for achieving the highest fundamental winding factor. From various coil materials [22] only aluminium and copper are considered. All stator DoF are given in Table 3.

Tables 1-3 fully define the specifications, constraints and the design DoF for all the considered machines.

3. Machine Modelling

3.1. Electro-Magnetic Model

The modelling process initiates with determination of rotor flux density ($\vec{B}$(x,y,z)) at all areas that are covered by machine windings. This field solely depends on rotor geometries and the distance between them, and can be calculated according to [23] for rotors with purely axial PMs containing a back iron, and according to [24] for ironless rotors with Halbach PMs. The rest of the modelling procedure is the same regardless of the rotor type. Once the B-field distribution is obtained, the armature current that is required to produce the desired torque can be obtained by employing the Lorentz force F,

$$\vec{T} = \vec{r} \times \vec{F} = \vec{r} \times (i \cdot \vec{l} \times \vec{B}), \quad (1)$$

where r is the distance between the conductor and the rotational axis, l is the conductor length and i is the phase current.

Only a force component in the tangential direction is capable of providing a torque. Thus, the previous expression becomes

$$T_\varphi = r \cdot F_\varphi = r \cdot i_r B_z l. \quad (2)$$

Based on (2), it is obvious that currents in directions other than radial (i_r) do not generate a torque-producing force. Hence, end windings, which only possess currents in the tangential direction, do not contribute to the torque.

The intensity of the B_z field varies in space. Moreover, it is time-dependent. From a stationary reference frame it can be perceived that it rotates at the angular velocity ω. At this point, it is useful to introduce the angle of rotation as

$$\theta = \omega \cdot t. \quad (3)$$

Based on (2), the expression for a torque produced by an infinitesimal fragment in stator phase a winding can be written as

$$dT_{a\varphi} = r \cdot \mathrm{d}F_{a\varphi} = r \cdot \frac{\pm i_{a,coil} \cdot \cos(\varphi)}{k_{Cu} \cdot c_\omega \cdot c_h} B_z(r, \varphi - \theta, z) \cdot \mathrm{d}V_a, \quad (4)$$

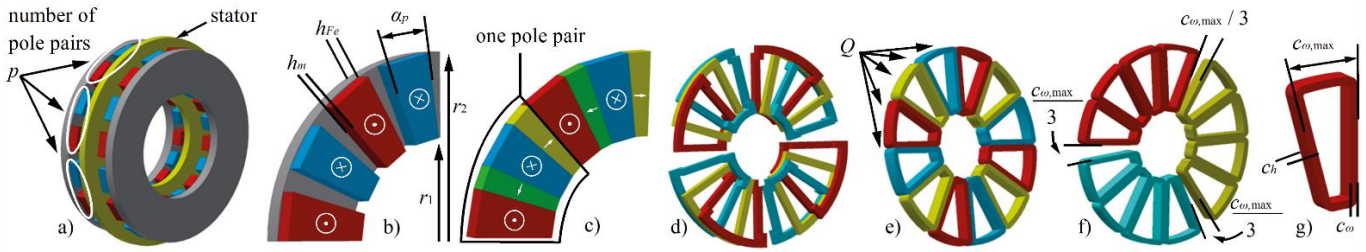

Fig. 2. a) *AFM with a single stator and two rotors,* ***b)*** *rotor (quarter view) employing purely axial PMs and a back iron,* ***c)*** *rotor employing PMs in Halbach configuration,* ***d)*** *stator formed of distributed windings (given for Q = 12),* ***e)*** *stator formed of traditional concentrated windings (given for Q = 12),* ***f)*** *stator formed of phase group concentrated windings (given for Q = 12),* ***g)*** *single stator coil. In Figs. 2d), 2e) and 2f) coils with the same colour belong to the same phase.*

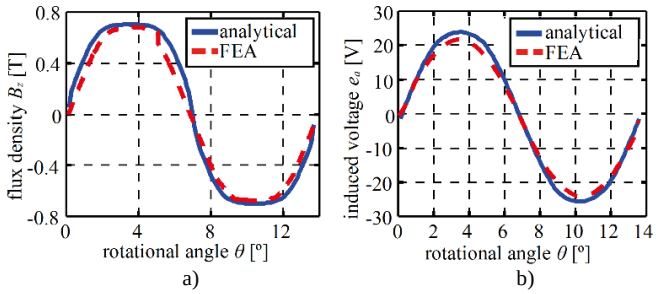

Fig. 3. ***a)*** *Distribution of axial field component B_z in the middle of the air gap,* ***b)*** *induced voltage (e_a) in AFM phase a at no-load operation, at the speed of 300 rpm.*

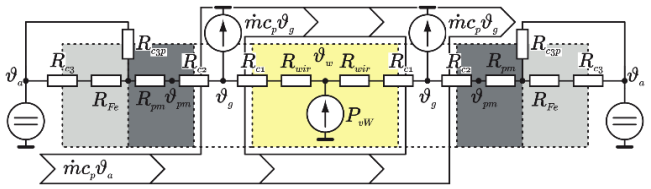

Fig. 4. *Thermal model of AFMs with two rotors. Convective thermal resistances R_{c1}, R_{c2}, R_{c3} and R_{c3p} encompass a space between ambient air and surfaces of: stator, PMs, back iron and rotor peripheral edge, respectively. Parameters $R_{\omega ir}$, R_{pm} and R_{Fe} stand for conduction thermal resistances of: windings, PMs and back iron, respectively. Temperatures ϑ_g, ϑ_a, ϑ_{pm}, and ϑ_ω stand for the air gap, ambient, permanent magnets and windings temperature, respectively. $P_{\vartheta W}$ and $\dot{m}$ stand for conduction losses and mass flow, respectively.*

where $i_{a,\,coil}$ is a sum of all currents that are flowing through a cross section of one coil from phase a, and $J_{a,\varphi} = \frac{\pm i_a \cdot \cos(\varphi)}{k_{Cu} \cdot c_\omega \cdot c_h}$ represents a radial component of this current's density. Angle φ is the angular distance of the observed point from a line that goes through the centre of the coil width. It is always in the range of $\arctan(\pm 0.5 c_\omega / r)$. Parameter k_{Cu} represents the coil fill factor, while c_ω and c_h are coil width and height (cf. Fig. 2g).

Spatial integration of infinitesimal torque components that are given by (4) leads to the overall torque that is produced by the machine phase a,

$$T_{a\varphi} = \iiint_{V_a} \mathrm{d}T_{a\varphi}, \tag{5}$$

where V_a represents a volume of active (radial) fragments of phase a coils (does not encompass end windings).

Assuming balanced, three-phase currents, the machine torque can be calculated as the average torque over the electrical period t_p,

$$T_{\varphi\,avg} = 3T_{a\varphi\,avg} = \frac{1}{t_p} 3 \int_{t=0}^{t=tp} T_{a\varphi} \mathrm{d}t \tag{6}$$

A desired average torque $T_{\varphi avg}$ and power are often given as requirements prior to the machine modelling process (here the power requirement was specified as 12.5 kW at 3200 rpm – Table 1). Now, all parameters from (4)-(6) are known, and the AFM current of the phase a can be obtained. From this current, stator conduction losses can be obtained as

$$P_{cond} = 3RI_{a\,rms}^2, \tag{7}$$

where the resistance R value can be calculated from coil dimensions. Since they are the most significant loss component in air-core AFM designs, only the conduction losses are considered for the efficiency calculation. Skin losses are not considered at this stage as they are highly dependent on numbers of parallel and series turns of the stator wire (which are determined only after the Pareto optimization). Eddy current losses in PMs are not considered as it would lead to inappropriately high increase in computational times.

An important machine performance indicator is the induced phase voltage e_a at no-load operation. This information can be extracted from the power balance equation that is given by

$$e_a \cdot i_a = T_{a\varphi} \cdot \omega, \tag{8}$$

where i_a is phase a current that flows through a single wire of a coil. From the induced voltage e_a, the flux linkage can be easily obtained by utilizing

$$e_a = -\frac{\mathrm{d}\psi_a}{\mathrm{d}t}. \tag{9}$$

The electro-magnetic models given in this section are validated by 3D FEM analysis by Ansys Electronics Desktop (Maxwell). A sample of the results is depicted in Fig. 3. It can be seen that the traces are matching with a peak error below 10%, which presents an adequate accuracy.

3.2. Thermal Model

Thermal models are indispensable in machine modelling for two reasons. The first one is that coils' resistances and remnant flux densities of PMs are temperature dependent. Therefore, only an iterative process simultaneously considering both the electro-magnetic (Section 3.1) and the thermal model can obtain machines' performances.

The second, and even more important reason, is to determine which machines would overheat during operation [25, 26] and to discard them. In this work, a machine is considered to overheat if it has coils' temperature above 125˚C. Therefore, all designs in which nominal current causes coil temperatures to exceed the limit are not viable machine designs.

The heat transfer in an AFM is studied in [6]. A lumped-parameter thermal network is presented in Fig. 4. The validity of the thermal model is considered as confirmed [6, 26]. The use of an air core stator leads to a constant air gap permeance and a weak armature reaction, consequently resulting in negligible rotor eddy-current losses. Other types of heat transfer to the rotor (e.g. from stator through bearings and machine shaft) have minor influence. Therefore, for the sake of simplicity, the rotor temperature is assumed to be the same as the air temperature in the air gap, which is much lower than temperatures required for a demagnetization of PMs [27]. Then, parameters in grey colouring in Fig. 4 can be neglected and the relevant part of the model becomes its inner part (coloured in yellow in Fig. 4). The remaining parameters are elaborated in what follows.

Thermal resistance between the stator centre and its

surface can be represented as

$$R_{\omega ir} = \frac{l}{4 \cdot A_{\omega ir} \cdot k}, \tag{10}$$

where $A_{\omega ir} = (r_2^2 - r_1^2)\pi$ is stator surface area, $l = 0.5 \cdot c_h$ (c_h is coil height – Fig. 2g), k is a mean thermal conductivity of the stator winding conductor and epoxy mixture. A uniform loss distribution is assumed (causing division by 4 [16]).

The convection resistance is defined by

$$R_c = \frac{1}{A_c \cdot h}, \tag{11}$$

where, based on [6] and [26],

$$h = \frac{k \cdot \overline{Nu}_{s,a}}{\bar{r}} \quad \text{and} \quad \overline{Nu}_{s,a} = 0.333 \frac{\dot{m}}{2\pi\nu\rho\bar{r}}. \tag{12}$$

Parameters ρ, ν and k are the air density, air kinematic viscosity and air thermal conductivity, respectively. The parameter $\dot{m}$ represents the air mass given by

$$\dot{m} = \dot{V} \cdot \rho, \tag{13}$$

where $\dot{V}$ is the volumetric flow rate. By taking into account AWT cruising speed, the volumetric flow rate is assumed here to have a value of 7 dm^3/s (Table 1).

Finally, the air temperature inside the air gap θ_g, and the stator temperature θ_s can be acquired from (14) and (15), respectively.

$$\frac{P_{loss,tot}}{2} = \dot{m} c_p (\theta_g - \theta_a) \tag{14}$$

$$\frac{\theta_s - \theta_g}{R_{\omega ir} + R_{c1}} = \dot{m} c_p (\theta_g - \theta_a) \tag{15}$$

3.3. Structural Model

Evaluation of structural weight of CL-AFMs is performed after their active (electro-magnetic) weight is assessed. The weight of passive components contributes to the overall weight of CL-AFM. Thus, it plays an important role in the optimization process. It is obtained as the minimal required weight which can lead to a design capable of withstanding three types of mechanical stress: torque (shear force), centrifugal (tensile) force and magnetic attractive force (bending stress). Small dimensions of the machine allow forces like gravity, thermal expansion and forces from the rotor blades [28] to be omitted from consideration. A potential weight reduction by utilization of magnetic bearings [29] is not here evaluated.

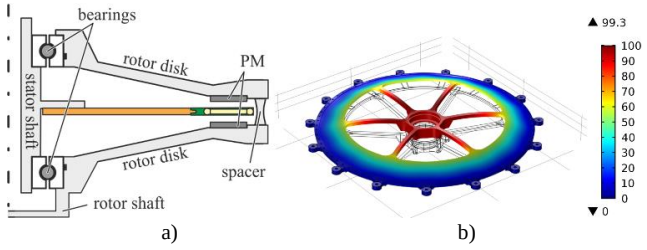

Fig. 5. ***a)*** *cross-sectional view of one half of the AFM, showing both electromagnetically active and inactive (purely structural) parts,* ***b)*** *FEM simulation showing bending stress on inner parts of AFM caused by attraction forces between opposing PMs.*

Initially, disk-shaped structures are considered to hold the rotor magnets (see Fig. 5a), whose dimensioning is done according to [30], resulting in a power density of 5.8 kW/kg (Fig. 6a). Then, rims were introduced (see Fig. 5b), and they were dimensioned by means of FEM analysis (in Comsol), resulting in the power density of 6.4 kW/kg.

4. Theoretical Results

Fig. 6a reveals the performances of all analysed machines, which are depicted as a single dot each. The figure is obtained as the fourth step of a procedure that is detailed in Section 2.

Machines that overheat during the operation are dyed in black, which indicates that they are not feasible designs. If all the machines with the same efficiency are compared, the best ones among them can be immediately identified as the ones located on the purple line denoted as the Pareto front, which represents a trade-off between the efficiency and the power-to- weight ratio.

Pareto fronts can also be utilized to compare different types of machines, as shown in Fig. 6b. They are obtained as the fifth step from Section 2.1. It is evident that machines with Halbach arrays outperform those with purely axially magnetized PMs and a back iron. This is a consequence of the fact that with the same weight they can produce higher flux density in the air gap. Post-processing revealed that optimal values of all DoF from Table 2 are higher than considered minimums and lower than considered maximums. The only exception is the number of pole pairs, for which 26 (which is chosen as a manufacturability limit) is shown to be the optimal value.

From Fig. 6b it can also be seen that CWs (Figs. 2e and 2f) allow superior performances compared to DWs (Fig. 2d). This is mainly due to their higher fill factor and shorter end windings. The best performance is achieved by PGCW (Fig. 6b).

It should be noted that the prototype machine has a much higher ratio (0.78) between disc's inner and outer radius than the value of 0.58 which is known to maximize a torque in machines with a fixed outer radius [31, 32]. However, this is very well justified by the fact that the optimization does not consider torque independently but together with the machine weight and efficiency.

Finally, the optimization results show that copper is always a better choice than aluminium for the winding material, as depicted in Fig. 6c. This is justified by the fact that aluminium has lower electrical conductivity. Thus, for the same current rating it demands a larger coil cross section area. Consequently, the distance between the two rotors increases.

The generation of a Pareto front does not mean that a globally optimum design is found, since the definition of optimum is application dependent. For airborne wind turbines, the design with 95% efficiency and 5.8 kW/kg power-to-weight ratio (6.4 kW/kg after fine-tuning by structural FEM simulations) is selected to be built as a prototype. It employs PMs in Halbach arrangement and

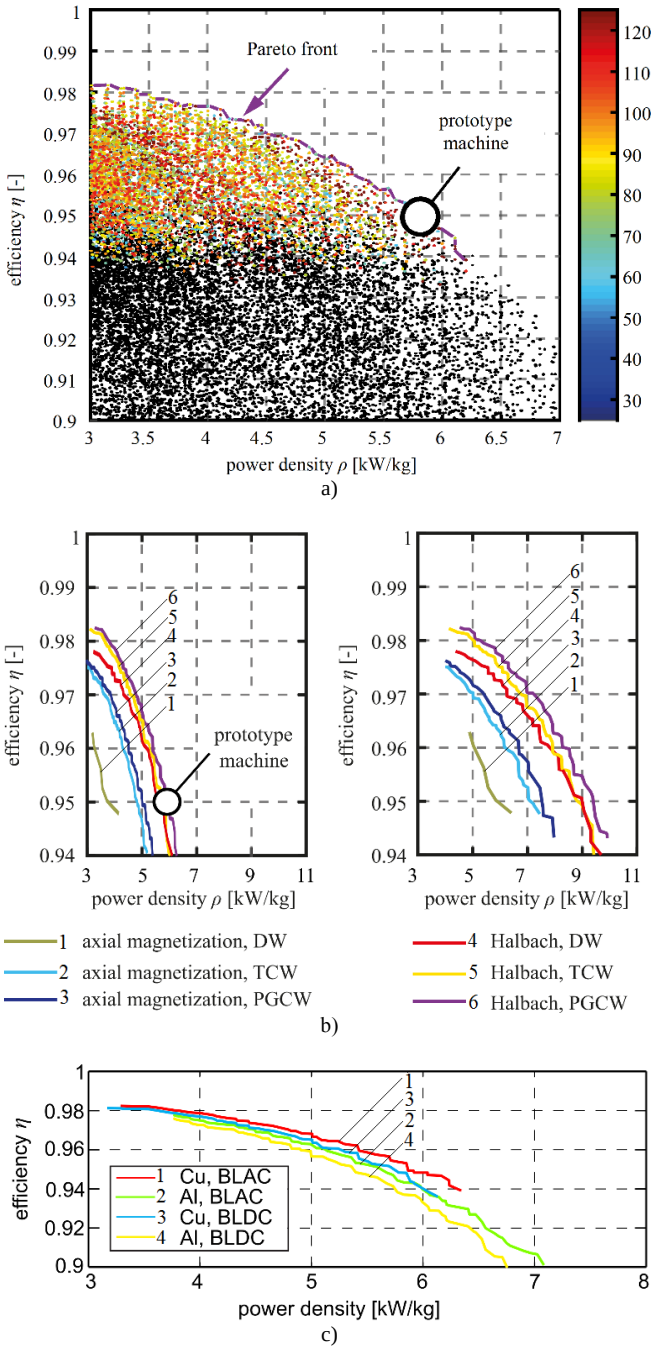

Fig. 6. *Theoretical results:* ***a)*** *Pareto graph of all CL-AFM types defined in Section 2. Each dot represents the performance of one unique CL-AFM. Back dots signify that their corresponding machines overheat during the operation.* ***b)*** *Pareto fronts of all CL-AFM types defined in Section 2. On the right hand side only the electro-magnetically active weight of the machines is considered. The graph on the left side considers the total weight including also purely structural parts.* ***c)*** *Comparison between Pareto fronts of CL-AFMs with different coil materials and different current waveforms.*

PGCW. Parameters that are specific to the selected machine are given in Table 4.

Together with Table 1, it provides sufficient information for the machine manufacturing, which is considered in the next section.

Table 4 Prototype machine

DoF	Chosen value (or designs)
Magnetization type	Halbach without iron (Fig. 2c)
Pole pair number [-]	$p = 26$
Disk inner radius [mm]	$r_1 = 90$
Disk outer radius [mm]	$r_2 = 115$
Permanent magnet height [mm]	$h_m = 4$
Pole coverage of axial magnets [-]	$\alpha_p = 0.6$
Winding type	Phase group concentrated (Fig. 2f)
Number of coils	$Q = 51$
Coil height [mm]	$c_h = 3$
Fractional coil width [-]	$c_{\omega,\mathrm{frac}} = 0.65$
Coil material	Copper
Current waveform	Sinusoidal (BLAC)

5. Manufacturing Process

5.1. Stator Manufacturing

The stator is formed of three parts: concentrated copper coils (Fig. 7a), an aluminium rim (CNC milled) and epoxy, which holds them stiffly together.

In order to produce the coils, at first, a tool for coil production is manufactured on a CNC machine. This tool positions and rotates a wire placed on it until a desired number of turns is obtained. Subsequently, the rolled wire is restrained at all sides and pressed. This prevents an occurrence of a thermal expansion during the heating process which follows. The heating is performed by applying a dc current through the winding. The heat melts a self-bonding layer of the wire, which, when it cools off, makes the coil stiff. A finished coil produced by the described process is shown in Fig. 7a.

The number of winding turns is selected as 12.5, to suite an inverter with a dc-link voltage of 800V. In order to accelerate the manufacturing process, no parallel conductors are utilized, and a single-layer foil winding (which is not an optimal solution) is chosen for the prototype machine. The selection of the most appropriate number of parallel and series turns (e.g. the use of multilayer coils and/or stranded conductors, which requires considering the trade-off between conduction and skin/proximity losses) is within the scope of future work.

In preparation for the potting process, finished coils together with the aluminium rim (whose sole purpose is keeping the stator mechanically stable) are placed in a sealed PTFE mould depicted in Fig. 7b. A vacuum pump is utilized to suck all the air out of the mould and the epoxy. This prevents formation of very harmful air bubbles in the stator which could cause thermal hot spots and a dielectric breakdown. When the barometer shows that a vacuum is formed, the epoxy (WEVOPOX 2513) can be let to flow into the mould. After the epoxy is cured, the process is finished. The obtained stator mounted on a shaft is presented in Fig. 7c.

5.2. Rotor Manufacturing

The two rotors of the CL-AFM are identical and each is composed of three parts: PMs, a CNC milled aluminium shield and a hybrid ceramic type ball bearing with a diameter of 35 mm.

In order to produce a Halbach array, PMs are at first put on a thin PTFE mould. An iron plate is placed below the PTFE mould for attracting the PMs and preventing them from

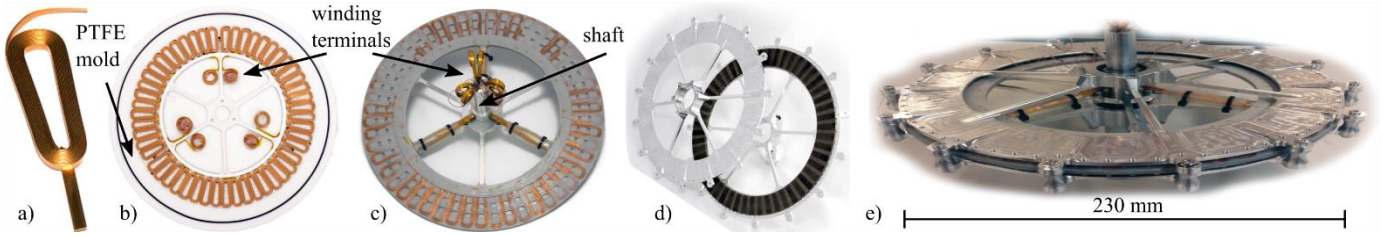

Fig. 7. *CL-AFM parts:* ***a)*** *a coil obtained using a custom made winding tool,* ***b)*** *stator coils positioned on a PTFE mould which is used for potting,* ***c)*** *stator after the potting process,* ***d)*** *two PM rotors,* ***e)*** *a completely assembled prototype machine.*

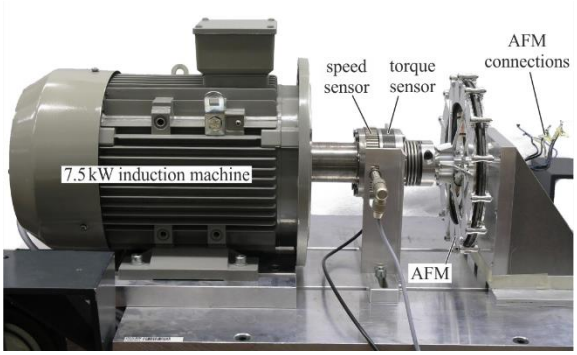

Fig. 8. *Experimental rig.*

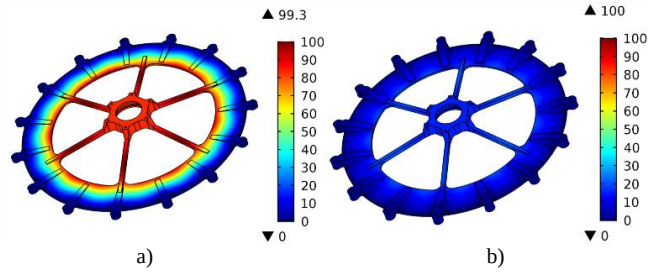

Fig. 9. *Analysis of the influence of height of structural elements on a bending stress of inner rotor parts. Rotor on the right features ten times lower bending with an increase of the total weight of only 6%.*

colliding with each other during the assembling process.

When all the PMs are placed on the mould, the aluminium shield is covered with a layer of epoxy (Loctite Hysol 9497) and placed on the top of them. A pressure is applied between the PTFE mould and the aluminium shield by clamps. The structure is left for 24 hours to cure at room temperature (20˚C), after which the rotor is finished (Fig. 7d). Fig. 7e depicts the fully assembled prototype CL-AFM. Its weight of m_{tot} = 2.065 kg perfectly matches the expected value obtained from simulations (2.075 kg).

6. Experimental Results

The machine test setup is depicted in Fig. 8. The prototype CL-AFM is mechanically coupled with a 7.5 kW induction machine (IM), which acts as the prime mover. The IM is supplied from a 7.5 kW Lust (Lti) converter (CDA34 series). The prototype AFM operates in the generator mode and converts the mechanical power into electrical power, which is further dissipated into heat on variable resistors that are attached to its stator winding terminals. The machine is tested without enclosure.

The transferred mechanical power is measured by Magtrol TF series torque flange sensor (TF 309-312), which also features a speed sensor (SPU210). The electrical power at the output of the prototype machine is measured by two synchronized Lecroy HDO4054 oscilloscopes.

It is known in literature that AFMs are challenging structures to assemble, particularly due to strong attractive forces acting on the rotors [33, 34]. Also in this work, some magnets were displaced under large attractive forces during the assembly process. This is attributed to bending of the rotor disk (especially its inner part), which in turn leads to the breaking of the glue holding the magnets. Therefore, in order to proceed with the verification of the design procedure under the minimal risk of mechanical failure, the air gap is increased to 2 mm (from 1 mm) in the following.

This, however, is not an unsolvable problem. The rotor bending had been predicted by the FEM model shown in Fig. 5b, but was tolerated since it did not lead to dangerous stress levels in the solid body. Fig. 9 depicts structural FEM simulations showing that the rotor bending can be almost nullified by a slight increase of the height of the 15 structural elements, which results in a mere 6% (128 grams) increase of the overall machine weight. Moreover, surface treating of the rotor disks and the magnets can increase the holding strength of the glue.

Regarding the experimental results in the following subsections, the only difference that the higher air gap causes is a lower flux linkage by 23% (as shown in Section 6.2). According to (8), the expected decrease in torque (and power) is proportional to it (i.e. 23%). Therefore, the results can be scaled to the air gap of 1 mm.

6.1. Machine Impedance

The impedances of the stator windings are measured with Agilent 4294A precision impedance analyser over a wide range of frequencies.

From Fig. 10, it can be seen that the measured inductances of the three phases are identical and equal to L_s = 76 μH. The dc resistance of the machine phases is obtained with a 4-wire resistance measurement on an Agilent 34410A 6½ Digit multimeter as R_s = 404 mΩ (at room temperature (20˚C)). The measured parameters are in good agreement with analytical models, which predicted them as R_s = 411 mΩ, L_s = 74 μH. It should be noted that at high speeds, the skin/proximity effect causes the machine resistance to be different from the dc resistance, which affects conduction losses.

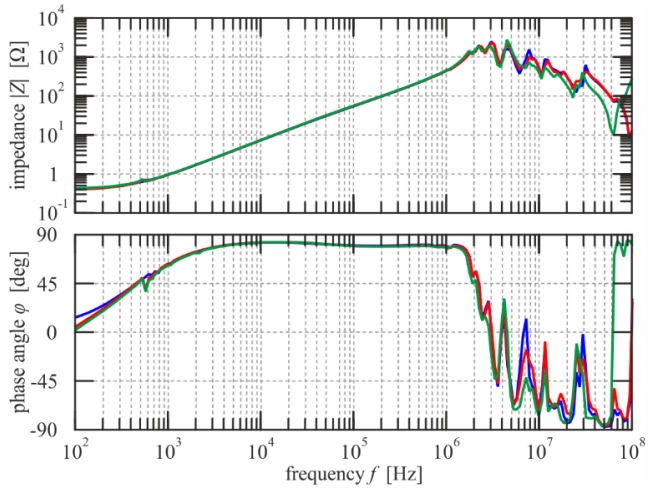

Fig. 10. *Stator windings impedance measurement (phases a, b and c).*

6.2. No-Load Test

In order to assess no-load losses in the prototype CL-AFM, its electrical terminals are left open and its shaft is rotated by an induction machine (IM), as shown in Fig. 8. The no-load losses are obtained from the speed and torque measurements on the shaft.

From Fig. 11a, it can be seen that the no-load losses are quadratically dependent on the speed (loss torque is linearly dependent on speed, which is represented by a mechanical frequency), from which it can be concluded that the windage losses are negligible compared to the sum of proximity (eddy currents in the windings) and bearing friction losses.

The segregation of the proximity and bearing friction losses, as well as the revisiting of the coil design to minimize the total (conduction plus skin/proximity) losses as detailed in [35] and detailed analysis of bearing losses as detailed in [34] are beyond the scope of this paper. However, a 2D FEM analysis shown in Fig. 11b depicts how proximity losses change with segmentation of coils. The segmentation would result in multilayer coils [36]. It is interesting to notice that a change from one to two layers (in axial direction) does not result in reduction of losses. This is explained by the fact that the transversal flux in the middle of the air gap is equal to zero.

Induced back EMF waveforms at 2700 rpm are shown in Fig. 12a. It can be seen that they are balanced and sinusoidal. Flux linkages with the air gap of 2mm and 1mm are calculated by integrating the voltage waveforms measured at 2700 rpm and 300 rpm, respectively (by applying (9)). They are depicted in Fig. 12b. They have an amplitude of 22.5 mWb, which validates the value predicted by the analytical models (22.6 mWb). Experimental results for the air gap of 1 mm (amplitude value of 29.1 mWb) are given on the same graph. They reveal that the higher air gap reduces the linked flux by 23%. This value is also verified by a simulation (whose results are here omitted).

6.3. Operation Under Load

In order to test the CL-AFM under a load, its electrical terminals are connected to a three-phase variable resistor while its shaft is driven by the IM. The results are shown in

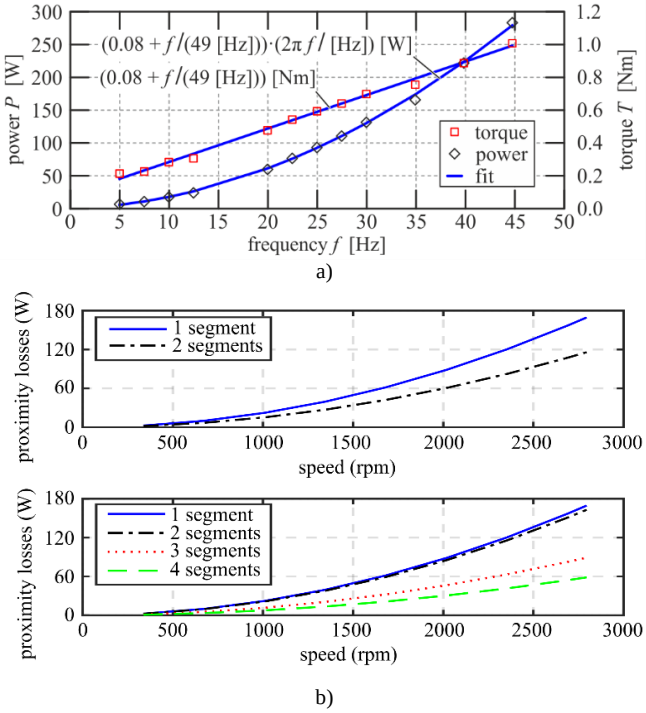

Fig. 11. ***a)*** *No-load test. The linear curve depicts measured torque, which is required in order to suppress no-load losses. A measured power of these losses is shown by the exponential curve. The frequency of 5 Hz corresponds to 300 rpm, and 45 Hz to 2700 rpm.* ***b)*** *FEM results showing how no-load proximity losses are affected by coil segmentation in transverse direction (upper graph) and axial direction (lower graph).*

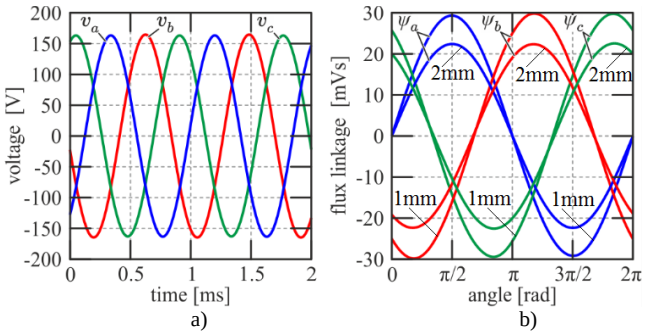

Fig. 12. ***a)*** *Measured induced phase voltages during no-load operation at 2700 rpm,* ***b)*** *flux linkage with the air gap of 2mm and 1mm.*

Fig. 13a for two constant speeds: 300 rpm and 600 rpm. As expected, the developed torque is linearly dependent on AFM current, and is not dependent on the machine speed. It can be seen that the experimental results are in very good agreement with calculations.

During the load operation at 3200 rpm, one magnet got detached from the rotor. The most probable reason for this is a slight unbalance in rotor's mechanical construction. Therefore, unlike no-load tests, load test results do not contain data at a full speed. For this reason, stating the rated power of the prototype machine is omitted here. However, as shown in Fig. 13a, the developed torque is speed invariant.

From Fig. 13a, it follows that the developed torque that is caused by the nominal current of 23.8 A rms is 29.7 Nm. Therefore, the input power at 3200 rpm is equal to

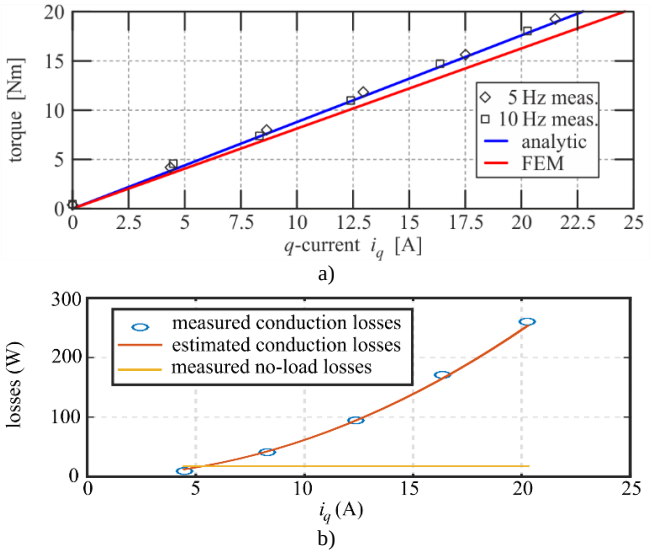

Fig. 13. ***a)*** *Torque dependence on q-current component at speeds of 300 rpm and 600 rpm. The graph contains a comparison between experimental (measured data), analytical and FEM data.* ***b)*** *Losses in the machine at a speed of 600 rpm. Comparison between measured and estimated (predicted by analytical model) conduction losses.*

9.95 kW, which scales to 12.87 kW for the air gap of 1 mm. By considering only conduction losses (686 W), an efficiency of 94.7% can be obtained for the air gap of 1 mm. The result is in good agreement with analytical results (Fig. 6a) which predicted it as 95%.

From Fig. 13b it can be seen that measured conduction losses match nicely with values that are predicted by the analytical model. Measured no-load losses, which are not part of the optimization algorithm, are shown on the same graph. Measured conduction losses are obtained by subtracting measured no-load losses (shown in Fig. 13b) and output power from a measured input power.

AFM phase voltage v_a and current i_a for the nominal current operation at the speed of 600 rpm are shown in Fig. 14a. A current density is 19.5 A rms/mm^2. As all machine parameters are known (Section 6.1), it is possible to obtain a back-EMF e_a (Fig. 14a) by adding a voltage drop on a measured voltage v_a. The impedance that the back EMF sees is a series connection of the machine impedance and the load impedance, both of which are resistive-inductive. Therefore, the current i_a lags the back EMF e_a.

D-q components of AFM phase voltages, currents and back-EMFs are given in Fig. 14b. It can be seen that the current *d*-component has a non-zero value for the reason described in the previous paragraph.

Finally, in Figs. 14c and 14d, the AFM input and output powers and torque and speed are depicted for the same operating point as the one described above.

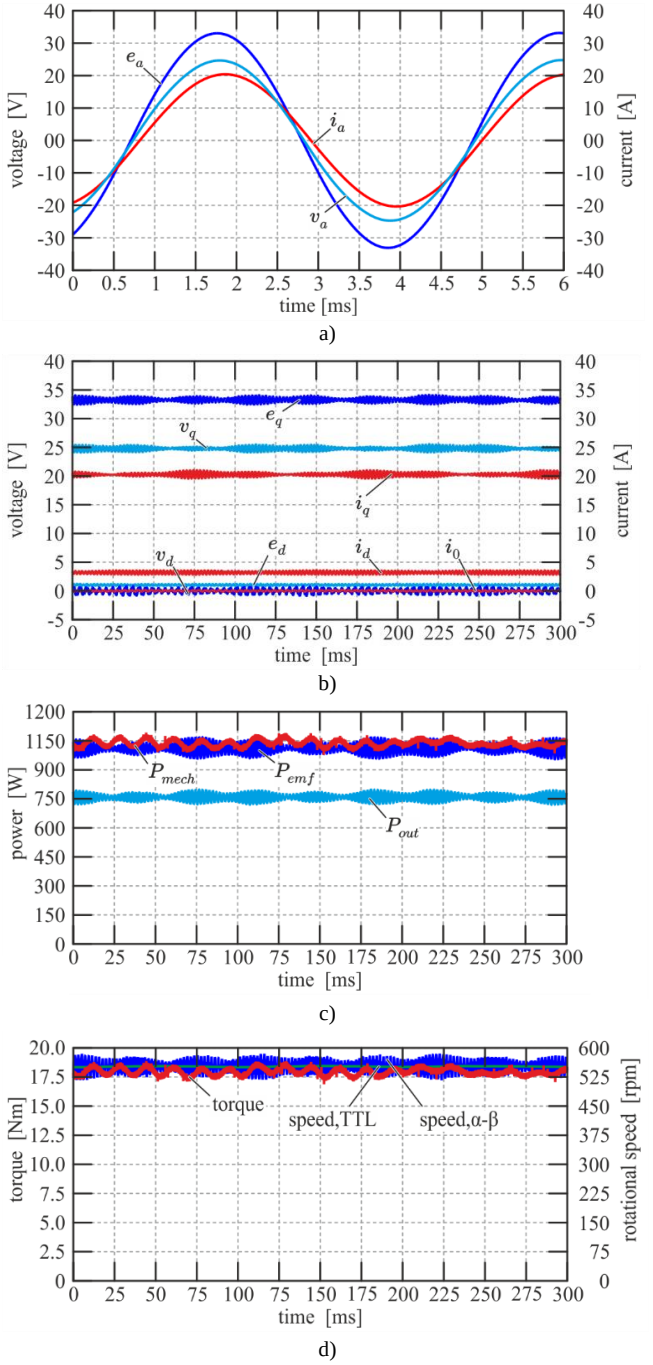

Fig. 14. ***a)*** *Measured AFM phase voltage v_a, current i_a, and back EMF e_a at the speed of 600 rpm.* ***b)*** *Measured d-q current components of AFM phase voltages, currents and back EMF.* ***c)*** *Measured AFM input power (P_{mech}), power transferred to stator (P_{emf}) and output power (P_{out}).* ***d)*** *Measured speed and torque.*

7. Conclusion

In this paper, a direct grid search optimization methodology which employs purely analytical and mutually dependent electro-magnetic, thermal and structural models is proposed. This allows a computationally efficient multi-objective Pareto-optimization of coreless axial-flux machines (CL-AFMs). The whole design space of CL-AFMs is considered, and performances of all the machines are revealed in a common (for all CL-AFM types) performance space. The clearly pronounced Pareto front is utilized to identify the optimal machine for a specific application, which is, in this case, an airborne wind turbine.

The selected AFM design yields a power-to-weight ratio of 6.4 kW/kg (2.9 kW/lb, 19 Nm/kg) at an efficiency of 95% and a rated speed of 3200 rpm (which is set as a constraint of the optimization process). The proposed optimization methodology and the claimed limits are experimentally verified on a prototype AFM. The prototypemachine is characterized by its high power-to-weight ratio and it is specifically built for this purpose. The experimental results confirmed the predicted performances

and the accuracy of the proposed multi-objective optimization methodology.

Un-modelled effects, like skin/proximity and mechanical losses, lower the efficiency at high speeds to well below theoretical 95%. They also decrease the power-to-weight ratio to well below theoretical 6.4 kW/kg. Moreover, the weight of additional structural parts providing additional mechanical strength, as discussed in Section 6, would further reduce the power-to-weight ratio by approximately 6%.

8. References

[1] Adhikari, J., and Panda, S.K.: 'Overview of high altitude wind energy harvesting system,' Proc. Of the 5th Int. Conf. on Power Electronics Systems and Applications (PESA), Hong Kong, China, 2013.

[2] Payne, P.R., and McCutchen, C.: 'Self-erecting windmill,' patent US 3987987A, 26 Oct. 1976.

[3] Makani Power, http://www.google.com/makani, accessed April 2018.

[4] Windlift Airborne Wind Energy Systems, http://windlift.com, accessed April 2018.

[5] Kolar, J.W., Friedli, T., Krismer, F., et al.: 'Conceptualization and multi-objective optimization of the electric system of an airborne wind turbine,' IEEE Journal of Emerging and Selected Topics in Power Electronics, 2013, 1, (2), pp. 73-103

[6] Gieras, J.F., Wang, R.J., and Kamper, M.J.: 'Axial flux permanent magnet brushless machines. 2nd edition,' (Springer, 2008).

[7] Siemens Press, http://www.siemens.com/press/en/feature/2015/corporate/2015-03-electromotor.php?content[]=Corp, accessed April 2018.

[8] Capponi, F.G., De Donato, G., and Caricchi, F.: 'Recent advances in axial-flux permanent-magnet machine technology,' IEEE Trans. on Ind. Applications, 2012, 48, (6), pp. 2190-2205

[9] Daghigh, A., Javadi, H., and Torkaman, H.: 'Design optimization of direct-coupled ironless axial flux permanent magnet synchronous wind generator with low cost and high annual energy yield,' IEEE Trans. on Magnetics, 2016, 52, (9), pp. 1-11

[10] Vun, S.T., and McCulloch, M.D.: 'Optimal design method for large-scale YASA machines,' IEEE Trans. on Energy Conversion, 2015, 30, (3), pp. 900-907

[11] Kahourzade, S., Mahmoudi, A., Ping, H.W., et al.: 'A comprehensive review of axial-flux permanent-magnet machines,' Canadian Journal of Elect. and Comp. Engineering, 2014, 37, (1), pp. 19-33

[12] Tüysüz, A., Zwyssig, C., and Kolar, J.W.: 'A novel motor topology for high-speed micro-machining applications,' IEEE Trans. on Ind. Electronics, 2014, 61, (6), pp. 2960-2968

[13] Kim, J.S., Lee, J.H., Song, J.Y., et al.: 'Characteristics analysis method of axial flux permanent magnet motor based on 2-D finite element analysis,' IEEE Trans. on Magnetics, 2017, 53, (6), pp. 1-4

[14] Virtič, P., Vražić, M., and Papa, G.: 'Design of an axial flux permanent magnet synchronous machine using analytical method and evolutionary optimization,' IEEE Trans. on Energy Conversion, 2016, 31, (1), pp. 150-158

[15] Sung, S.Y., Jeong, J.H., Park, Y.S., et al.: 'Improved analytical modeling of axial flux machine with a double-sided permanent magnet rotor and slotless stator based on an analytical method,' IEEE Trans. on Magnetics, 2012, 48, (11), pp. 2945-2948

[16] Gammeter, C., Drapela, Y., Tüysüz, A., et al.: 'Weight optimization of a machine for airborne wind turbines,' Proc. of the 40th IEEE Ind. Electronics Society Conf. (IECON), Dallas, Texas, 2014.

[17] Subotic, I., Gammeter, C., Tüysüz, A., et al.: 'Weight optimization of an axial-flux PM machine for airborne wind turbines,' Proc. of IEEE Int. Conf. on Power Electronics, Drives and Energy Systems (PEDES), Trivandrum, India, 2016.

[18] Jaksic, D.: ' "Getting rid of the air", or how to maximize winding fill factor (ID 81),' Proc. of the 1st Int. Electric Drives Production Conf., Nuremberg, Germany, 2011.

[19] Husain, T., Tekgun, B., Sozer, Y., et al.: 'Comparison of axial flux machine performance with different rotor and stator configurations,' Proc of IEEE Int. Electric Machines and Drives Conf. (IEMDC), Miami, Florida, 2017.

[20] Fawzal, A.S., Cirstea, R.M., Gyftakis, K.N., et al.: 'Fan performance analysis for rotor cooling of axial flux permanent magnet machines,' IEEE Trans. on Ind. Applications, 2017, 53, (4), pp. 3295-3304

[21] Xia, B., Shen, J.X., Luk, P.C.K., et al.: 'Comparative study of air-cored axial-flux permanent-magnet machines with different stator winding configurations,' IEEE Trans. on Ind. Electronics, 2015, 62, (2), pp. 846-856

[22] Rallabandi, V., Taran, N., Ionel, D.M., et al.: 'Coreless multidisc axial flux PM machine with carbon nanotube windings,' IEEE Trans. on Magnetics, 2017, 53, (6), pp. 1-4

[23] Huang, Y., Ge, B., Dong, J., Lin, H., et al.: '3-D analytical modeling of no-load magnetic field of ironless axial flux permanent magnet machine,' IEEE Trans. on Magnetics, 2012, 48, (11), pp. 2929-2932

[24] Thompson, W.K.: 'Three-dimensional field solutions for multi-pole cylindrical Halbach arrays in an axial orientation,' Report, NASA Glenn Research Centre, Cleveland, Ohio, 2006.

[25] Chong, Y.C., Subiabre, E.J.P.E., Mueller, M.A., et al.: 'The ventilation effect on stator convective heat transfer of an axial-flux permanent-magnet machine,' IEEE Trans. on Ind. Electronics, 2014, 61, (8), pp. 4392-4403

[26] Howey, D.A., Childs, P.R.N., and Holmes A.S., 'Air-gap convection in rotating electrical machines,' IEEE Trans. on Ind. Electronics, 2012, 59, (3), pp. 1367-1375

[27] De Bisschop, J., Vansompel, H., Sergeant, P., et al.: 'Demagnetization fault detection in axial flux PM machines by using sensing coils and an analytical model,' IEEE Trans. on Magnetics, 2017, 53, (6), pp. 1-4

[28] Mcdonald, A.S., Mueller, M.A. and Polinder, H.: 'Structural mass in direct-drive permanent magnet electrical generators,' IET Renewable Power Generation, 2008, 2, (1), pp. 3-15

[29] Shrestha, G., Polinder, H., Bang, D. and Ferreira J.A.: 'Structural flexibility: a solution for weight reduction of large direct-drive wind-turbine generators,' IEEE Trans. on Energy Conversion, 2010, 25, (3), pp. 732-740

[30] Mueller, M.A., McDonald, A.S., and Macpherson, D.E.: 'Structural analysis of low-speed axial-flux permanent-magnet machines,' IEE Proc. - Electric Power Applications, 2005, 152, (6), pp. 1417-1426

[31] Mahmoudi, A., Rahim, N.A., and Ping, H.W.: 'Axial-flux permanent-magnet motor design for electric vehicle direct drive using sizing equation and finite element analysis,' Progress in Electromagnetics Research, 2012, 122, pp. 467-496

[32] Baker, J.L., and Mellor, P.H.: 'Influence of stator split-ratio upon the thermally limited power-envelope of a permanent-magnet electrical machine,' Proc. of IEEE Int. Electric Machines and Drives Conference (IEMDC), Miami, Florida, 2017.

[33] Di Gerlando, A., Foglia, G.M., Iacchetti, M.F., et al.: 'Effects of manufacturing imperfections in concentrated coil axial flux PM machines: evaluation and tests,' IEEE Trans. on Ind. Electronics, 2014, 61, (9), pp. 5012-5024

[34] Wrobel, R., Vainel, G., Copeland, C., et al.: 'Investigation of mechanical loss components and heat transfer in an axial-flux PM machine,' IEEE Trans. on Ind. Applications, 2015, 51, (4), pp. 3000-3011

[35] van der Geest, M., Polinder, H., Ferreira, J.A., et al.: 'Current sharing analysis of parallel strands in low-voltage high-speed machines,' IEEE Trans. on Ind. Electronics, 2014, 61, (6), pp. 3064-3070

[36] Rallabandi, V., Taran, N., and Ionel, D.M.: 'Multilayer concentrated windings for axial flux PM machines,' IEEE Trans. on Magnetics, 2017, 53, (6), pp. 1-4